SAND2017-3736J

Electronic and Thermoelectric Properties of Crystalline 2D Metal-Organic Frameworks

Yuping He, Catalin D. Spataru, François Léonard*, Reese E. Jones, Michael E. Foster, Mark Allendorf and A. Alec Talin*
Sandia National Laboratories, Livermore, California 94551, United States

* yuphe@sandia.gov and fleonar@sandia.gov

ABSTRACT

Two-dimensional materials have attracted much attention due to their novel properties. An exciting new class of 2D materials based on metal-organic frameworks (MOFs) has recently emerged, displaying high electrical conductivity, a rarity among organic nanoporous materials. The emergence of these materials raises intriguing questions about their fundamental electronic, optical, and thermal properties, but few studies exist in this regard. Here we present a fundamental study of the thermoelectric properties of the crystalline 2D MOFs $X_3(HITP)_2$ with X = Ni, Pd or Pt, and HITP = 2,3,6,7,10,11-hexaiminotriphenylene, calculated using *ab initio* simulations. We explore the dependence of thermoelectric transport properties on the atomic structure by comparing the calculated band structure, band alignment, and electronic density of states of the three 2D MOFs, and find that the thermoelectric transport properties strongly depend on the interaction between the ligands and the metal ions, in addition to the d orbital splitting of the metal ions induced by the ligands. Furthermore, unlike n-type doping, a significant deviation from the Wiedemann-Franz law arises in these materials for p-type doping, with a non-linear behavior of the Lorentz number as a function of hole concentration. The results show that thermoelectric transport properties of $X_3(HITP)_2$ systems could be enhanced by substituting heavy metal ions to increase the interaction between the metal ion and the ligands.

The results of this work provide fundamental guidance to optimize the existing 2D MOFs, and to design and discover new families of MOF-like materials for thermoelectric applications.

Keywords: metal-organic framework, thermoelectrics, thermal conductivity, energy conversion

TOC

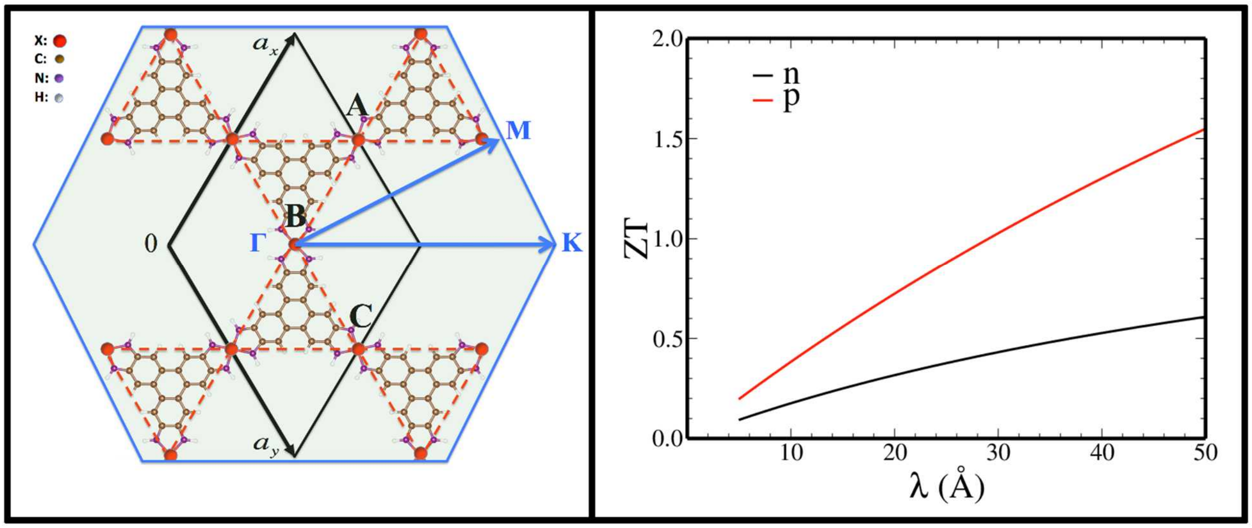

INTRODUCTION

Controlling the physical dimensionality of materials has led to profound new scientific discoveries and entirely new possibilities for electronic and optoelectronic applications. In particular, two-dimensional (2D) materials, such as graphene and transition metal dichalcogenides (TMDCs), have spurred much research across scientific and technological disciplines[1-5]. A recent trend has been to broaden the suite of 2D materials, for example with TMDC alloys[6, 7]. In this regard, a fundamentally new development has occurred whereby metal-organic frameworks (MOFs), which are usually three-dimensional and electrically insulating, have recently been synthesized in 2D layered form with high electrical conductivity[8]. This development opens a breadth of scientific questions about their fundamental properties, as well as their potential for applications. To date, only a few theoretical studies have appeared and addressed the fundamental electronic properties of these novel 2D materials[9-11]; in particular, the thermoelectric (TE) properties have not been discussed despite their importance as a diagnostic of material properties, and for potential energy applications.

Thermoelectric devices convert heat into electricity, or vice versa, without any moving parts, and are therefore attractive for energy harvesting and electronic cooling [12, 13]. The efficiency of a TE device is determined by the material figure of merit $ZT = S^2\sigma T/(\kappa_e + \kappa_L)$, where T is the absolute temperature, S the Seebeck coefficient, σ the electrical conductivity, and κ_e and κ_L are the electronic and lattice thermal conductivities, respectively. Although the ZT of commercial TE materials (i.e. Bi_2Te_3) is about 1, there is no known theoretical upper limit of ZT[14]. A high value of ZT could be achieved for materials with phonon-glass and electron-crystal properties[15]. However, it has been a challenging task to find materials with high ZT due to the competing interplay between S, σ, κ_e, and κ_L[13]. In addition to searching for materials with high ZT, discovering low-cost, high-performance, flexible, and environmentally friendly TE materials is crucial to accelerate the commercialization of TE devices.

Organic polymers have recently emerged as promising materials for TE applications[16-19], with ZT values as high as 0.42 at room temperature[20]. Conducting organic polymers are intrinsic phonon-glass materials with a small thermal conductivity comparable to inorganic amorphous materials[21]. For example, poly(3,4-ethylenedioxythiophene) doped with polystyrene sulphonic acid (PEDOT:PSS) has a thermal conductivity of 0.2 W/mK[22], and highly doped polyacetylene has a value of 0.7 W/mK[23]. However, their low electrical conductivity has been limiting the ZT to values below 1. It is necessary, therefore, to explore other organic materials with both low thermal conductivity and high electronic conductivity. Metal-organic frameworks (MOFs) consisting of metal ions interconnected with organic ligands typically have low thermal conductivities owing to their high density of nanopores, but are usually poor electrical conductors due to the redox-inactive organic ligands and limited overlap between their π orbitals and the d orbitals of the metal ions. Interestingly several MOFs with electrical conductivity ranging from ~10^{-7} to 10^1 S/cm have recently been obtained[8, 24-27]. In particular, Sheberla et al. [8] reported a 2D graphene-like semiconducting MOF, $Ni_3(HITP)_2$ (HITP=2,3,6,7,10,11-hexaiminotriphenylene), with conductivity values of 2 and 40 S/cm for bulk and thin films, respectively. A few theoretical works have been carried out to understand and predict the unusual properties of these 2D MOFs[9, 10]. For example, the quantum anomalous Hall state was predicted in 2D $X_3(HITP)_2$ with X=Ta, Re, or Ir[9], and a 3D $Cr_3(HITP)_2$ with a large band gap could potentially be produced by inserting a spacer linker between the layers[10]. However, a theoretical study of electronic and thermoelectric transport properties of these materials is still missing. Understanding the TE properties is important both from a fundamental scientific perspective as well as with regards to possible future applications in TE devices.

In this context, we present an investigation of the TE transport properties of three 2D MOFs: $Ni_3(HITP)_2$, $Pd_3(HITP)_2$ and $Pt_3(HITP)_2$, using a combination of *ab initio* simulations and the Landauer formalism. We carried out a series of *ab initio* calculations (i.e. electronic band structure, band alignment and partial density of states) and computed the TE transport properties (i.e. Seebeck coefficient, electrical conductivity and electronic thermal conductivity) of these 2D MOFs. The aim of this theoretical study is to understand the influence of the intrinsic material properties on the TE efficiency at the atomic scale, in particular the interaction of metal ions and organic ligands. We show that the coupling between the d_{xz} and d_{yz} orbitals of the metal ions and the p_z orbitals of C and N mainly determines the behavior of TE transport properties. We predict that $Pt_3(HITP)_2$ could be a better TE material than $Ni_3(HITP)_2$ and $Pd_3(HITP)_2$, especially for p-type doping, owing to the strong interaction between the d orbitals of Pt metal ions and the p orbitals of C and N. The findings of this work on 2D MOFs are also relevant to an improved understanding of the electronic transport properties of the broader class of MOFs materials.

RESULTS AND DISCUSSION

Electronic structure. Experimental data has shown that the 2D crystal structure of $Ni_3(HITP)_2$ is hexagonal with the in-plane lattice constants of $a_x = a_y = 21.75$ Å [8]. Figure 1a shows a schematic diagram of its atomic arrangement in the unit cell along the X and Y directions and its first Brillouin zone with the high symmetry points Γ, K and M. Using an *ab initio* method based on density functional theory (DFT) within the local density approximation (LDA) for electron interactions (see Methods), we optimized the monolayer hexagonal structures of $X_3(HITP)_2$ with X=Ni, Pd, or Pt starting with the experimental structure data of $Ni_3(HITP)_2$. The optimized lattice constants of $Ni_3(HITP)_2$ are $a_x = a_y = 21.32$ Å (i.e. ~2% smaller than experimental values). We find that the optimized lattice constants of $Pd_3(HITP)_2$ and $Pt_3(HITP)_2$ are systematically larger than those of $Ni_3(HITP)_2$ due to the increasing ionic radii of the metal ions (see Table I).

Using the optimized atomic structures, we carried out a series of *ab initio* electronic structure calculations. We first calculated the electronic band structure along the high symmetry points Γ, K, and M. Figure 2a-c show the band structures in the energy range of -1 eV to 1 eV for the three MOFs. An indirect bandgap increases as the metal ion changes from Ni to Pd, and Pt. Since the LDA functional generally underestimates the bandgap of semiconductors, we also calculated the bandgaps using the hybrid functional HSE06. As expected, we find that the band gaps calculated at the HSE06 level are larger than those obtained with LDA, and reach values between 0.25 eV and 0.42 eV (see Table I). These small bandgaps are quite interesting from a MOF perspective, because MOFs typically show band gaps of several eVs[28]. Even more interesting is the clear conduction and valence band dispersion, implying that the electronic carriers of these 2D MOFs have non-zero transport velocities. Moreover, while the conduction band dispersion is similar for the three MOFs, the valence band dispersion is significantly enhanced by replacing Ni with Pd and Pt metal ions. These results indicate that $Pd_3(HITP)_2$ and $Pt_3(HITP)_2$ could be better p-type conductive materials compared to $Ni_3(HITP)_2$.

We then calculated the partial density of states contributed from different species within the energy range of -0.3 to 0.3 eV. As shown in Fig. 2d-f, the valence band in all three MOFs is composed of orbitals from both ligands (i.e. *p* orbitals of C and N) and metal ions (i.e. *d* orbitals of Ni, Pd and Pt), but the conduction band composition is slightly different in each system. For example, the conduction band minimum (CBM) in $Ni_3(HITP)_2$ is dominated by the Ni *d* orbitals, but in the $Pd_3(HITP)_2$ system it is governed by the Pd *d* orbitals and the N *p* orbitals. On the other hand, in $Pt_3(HITP)_2$, it is constituted from the Pt *d* orbitals and the C and N *p* orbitals. In addition, as the metal ion changes from Ni to Pd and Pt, not only are the contributions of the metal ion *d* orbitals to the conduction band increasing, but their contribution to the valence band also increases. In $Pt_3(HITP)_2$, we find that the *d* orbitals of Pt appear to lead the valence band, instead of the orbitals from the ligands in the case of $Ni_3(HITP)_2$.

According to crystal field theory, the *d* orbital splitting of metal ions is primarily determined by the symmetry of ligands around the central metal ion. In the 2D MOFs of $X_3(HITP)_2$, there are four ligands around the metal X. Therefore, we expect that the metal X has a square planar splitting which contains four different energy levels: $d_{x^2-y^2} > d_{xy} > d_{z^2} > d_{xz} = d_{yz}$. To understand the *d* orbital splitting of Ni, Pd and Pt, and their interactions with the ligands (HITP), we calculated and compared the partial density of states contributed from the *d*_orbitals of Ni, Pd and Pt. We find that only the d_{xz} and d_{yz} orbitals contribute to the conduction and valence bands in all three MOFs, regardless of metal species. The other *d* orbitals (i.e. $d_{x^2-y^2}$, d_{xy} and d_{z^2}) form bonding and antibonding bands with energies far from the middle of the band gap. In addition, going down the group 10 elements, the *d* orbitals become more extended and overlap each other, especially for the HOMO bands, indicating a large interaction between metal ions and the ligands. This is a well-known trend in coordination chemistry[29].

To further illustrate the interaction between metal ions and organic ligands, we drew a band alignment diagram for each MOF system based on the calculated partial density of states (see Fig. 1b). We extract the energy levels of the *d* orbitals of metal ions and the *p* orbitals of C and N, which contribute to the valence band maximum (VBM) and CBM. We find that only the p_z orbitals of N and C form π-bonds with the d_{xz} and d_{yz} orbitals of the metal ions due to their same odd parity under mirror symmetry about the XY plane, consistent with a recent study[9]. As shown in Fig. 1a, there are three metal ion sites in the unit cell of $X_3(HITP)_2$, which we denote as A, B, and C. The metal ion at each site has two orbitals (i.e. d_{xz} and d_{yz}) forming π-bonds with the p_z orbitals of N and C, indicating that there could be six *d* orbitals contributing to the VBM and CBM (i.e. $\mathrm{d}_{xz}^{\mathrm{A,B,C}}$ and $\mathrm{d}_{\mathrm{yz}}^{\mathrm{A,B,C}}$). However, we find that the number of orbitals dominating the VBM and CBM varies in the three MOFs, leading to a very different band alignment in each system. The p_z orbitals of both C and N contribute to the VBM in all three MOFs, while their contributions to the CBM depend on the number of *d* orbitals of the metal ions. For example, in $Ni_3(HITP)_2$, the CBM is formed by one Ni *d* orbital (i.e. $\mathrm{d}_{\mathrm{yz}}^{\mathrm{A}}$), but has no contribution from the orbitals of ligands. On the other hand, in the case of $Pd_3(HITP)_2$, the CBM contains three Pd *d* orbitals (i.e. $\mathrm{d}_{\mathrm{yz}}^{\mathrm{A,B,C}}$) and also one N p_z orbital, while the CBM of $Pt_3(HITP)_2$ is composed of five Pt *d* orbitals (i.e. $\mathrm{d}_{xz}^{\mathrm{B,C}}$ and $\mathrm{d}_{\mathrm{yz}}^{\mathrm{A,B,C}}$) and two p_z orbitals from both N and C. Since the metal ions bind to the same ligands in all three MOFs, one may expect them to have the same levels of *d* orbital splitting. However, we find that the different metal ions result in different *d* orbital splittings, indicating that the *d* orbital splitting may also depend on the interaction of metal ions and ligands. The results of both partial density of states and band alignment demonstrate that the interaction between metal ion and ligands increases as the metal ion changes from Ni to Pd and

Pt. This is likely responsible for the obtained different bandgaps and band dispersions among the three MOFs, which in turn determines the electronic and thermal transport properties.

Thermoelectric properties. Having understood the basic electronic structure properties of 2D X_3(HITP)$_2$, we now discuss their thermoelectric transport properties. We employed the Landauer approach[30-32] to calculate the electronic conductivity, Seebeck coefficient, and electronic thermal conductivity using the full band electronic structure obtained from the *ab initio* calculations. These quantities were calculated for perfect crystalline materials, neglecting point defects or grain boundaries. Even in structurally perfect materials, other intrinsic mechanisms (e.g. electron-phonon scattering) may lead to electron scattering and diffusive transport determined by a mean-free path λ. In this work, we treat λ as an unknown parameter, which can be determined computationally or experimentally. In this case, the calculated Seebeck coefficient is independent of λ, and the calculated electrical conductivity and electronic thermal conductivity are proportional to λ (see Methods). Although λ could change the absolute values of the calculated transport properties, it does not change the systematic behavior of transport properties among the three 2D MOFs.

Figure 3a and b show the calculated Seebeck coefficient as a function of carrier concentration at room temperature. For all three materials, we find the standard behavior for semiconductors, namely a negative (positive) S for n-type (p-type) doping with large peaks at lower carrier concentrations. In addition, the general expectation that S scales with the semiconductor bandgap is also followed for these MOFs, i.e. S[Pt_3(HITP)$_2$] > S[Pd_3(HITP)$_2$] > S[Ni_3(HITP)$_2$] [33]. The behavior of S can also be understood from the calculated density of states (DOS) with the usual expression $S \sim D'(E)/D(E)\big|_{E_F}$; indeed, while in all three cases the variation of the DOS with energy is similar, there is a systematic increase in the DOS as the metal ion is changed from Ni to Pd and Pt (see Fig. 2), leading to a larger S. The different values of S between n-type and p-type doping at the same doping concentration is due to the variation of $D'(E)$ for the valence and conduction bands. The maximum value of the Seebeck coefficient (~600 μV/K) can be compared with bulk materials with similar bandgaps. For example, Bi_2Te_3 has a bandgap of 0.2 eV, and attains a maximum S of 300 μV/K at room temperature[32]. Similar comparisons can be made with other 2D materials: graphene has a maximum S of 50 μV/K[34], while MoS_2 has been shown to be as high as 30 mV/K[35].

The electronic conductivity is determined by the number of transport modes available around the Fermi energy (i.e. the product of carrier velocity and density of states), which can be directly related to the band dispersion. As such, we find that the n-type electronic conductivities are similar for all three MOFs, while for p-type doping it follows the trend $\sigma[Pt_3(HITP)_2] > \sigma[Pd_3(HITP)_2] > \sigma[Ni_3(HITP)_2]$. These results are consistent with the conduction and valence band dispersions (see Fig. 2). Since the number of modes increases with increasing energy away from the band edges, the electrical conductivity increases monotonically with increasing n-type and p-type doping. However, we found that the electronic thermal conductivity is monotonic with n-type doping for all three MOFs, but non-monotonic with p-type doping, which raises a question about the validity of Wiedmenann-Franz law for these p-type systems.

In the case of metals at high temperature, the Wiedemann-Franz (WF) law $\kappa_e / \sigma = L_0 T$, where L_0 is the Lorenz number (~2.4×10^{-8} WΩ/K^2), is a good description of the relation between electrical conductivity (σ) and electronic thermal conductivity (κ_e). This expression is often used to infer the electronic component (κ_e) of the total thermal conductivity since it can be difficult to measure it independently from the phonon thermal conductivity. It is thus important to assess the validity of this expression for specific materials, especially since the assumptions used to derive the WF law are quite specific. To address this question, we estimated the Lorenz number for n-type and p-type doped MOFs in this study using the calculated κ_e and σ at T=300 K. As shown in Fig. 4a and 4b, we find that the WF law is valid for n-type doping at high carrier concentration for all three MOFs (i.e. the effective Lorentz number L~2.3×10^{-8} WΩ/K^2), but it is significantly different for p-type doping at the same concentration level as that of n-type. In the case of p-type doping, the L of both Ni and Pd MOFs is non-linear as a function of hole concentration. Although the effective Lorentz number L of the Pt MOF saturates to a constant value at high concentration, it is much smaller than L_0 (i.e. $L \sim 0.5 \times 10^{-8}$ WΩ/K^2). We find that the behavior of L with n-type and p-type doping is similar to the calculated DOS (see Fig. 2), indicating that the validity of the WF law is determined by the number of charge carriers around Fermi level.

The power factor ($PF=S^2\sigma$) is a quantity that represents the performance of electronic transport in TE materials. Figures 3g and 3h show the calculated *PF* of the three MOFs for n-type and p-type doping, respectively. Since *S* decreases and σ increases as carrier concentration increases, there is a maximum value of *PF* at a certain carrier concentration. We find that for all three MOFs, the best performance with n-type carriers is for a doping concentration of ~$2\text{x}10^{12}$ cm^{-2}, while with p-type carriers, it is ~$5\text{x}10^{12}$ cm^{-2}. In the case of n-type doping, the *PF* of the Pt MOF is slightly larger than those of Ni and Pd, while for p-type doping, we find a significant difference with *PF*[$Pt_3(HITP)_2$] > *PF*[$Pd_3(HITP)_2$] > *PF*[$Ni_3(HITP)_2$]. Overall, the performance of electronic transport in the p-doped regime is better than that of the n-doped regime, except for the Ni MOF, in which the n-doped transport properties appear to be better. The best TE material among the three MOFs is $Pt_3(HITP)_2$ for both n-type and p-type doping, which can be understood from the *ab initio* electronic structure calculations showing that the Pt MOF has a larger bandgap, more band dispersion, and stronger overlap between the Pt ion and the ligands.

As mentioned in the introduction, the efficiency of TE materials is determined by the quantity $ZT = PF \bullet T / \kappa_T$, which depends on both electronic transport (i.e. *PF*) and thermal transport (i.e. $\kappa_T = \kappa_e + \kappa_L$) at a given T. To understand the TE efficiency of these 2D MOFs, we estimate the ZT of $Pt_3(HITP)_2$ as a function of mean free path (λ) of carriers at room temperature using the maximum value of PF and $\kappa_T = \kappa_e^{'}\lambda + \kappa_L$ for both n-type (n~$2\text{x}10^{12}$ cm^{-2}) and p-type (p~$5\text{x}10^{12}$ cm^{-2}) doping. $\kappa_e^{'} = \kappa_e / \lambda$ was calculated using the Landauer formalism (see Fig. 3). The value of $\kappa_e^{'}$ is ~$1.25\text{x}10^4$ $\text{WK}^{-1}\text{cm}^{-2}$ for electrons at the concentration n~$2\text{x}10^{12}$ cm^{-2}, and ~$6.28\text{x}10^3$ $\text{WK}^{-1}\text{cm}^{-2}$ for holes at the concentration p~$5\text{x}10^{12}$ cm^{-2}. We obtained the phonon thermal conductivity κ_L~1 $\text{WK}^{-1}\text{m}^{-1}$ from classical molecular dynamic simulation using the Green Kubo approach (see Methods) applied to perfect crystals. Given the absence of defects which scatter phonons and, hence, reduce the mean free path, this value of κ_L is an upper bound, and therefore the estimated value of ZT is a lower bound. As shown in Fig. 5, ZT is almost linearly proportional to λ, and ZT for p-type doping is systematically larger than that for n-type doping. Furthermore, relevant values of ZT can be achieved provided the electronic mean-free path is larger than a few nanometers. These results show that synthesizing 2D MOFs with a high degree of crystallinity and purity is a promising approach to developing novel TE materials.

CONCLUSION

In summary, we carried out a series of *ab initio* calculations to understand the electronic and thermoelectric properties of the $X_3(HITP)_2$ 2D MOFs with X=Ni, Pd and Pt. We employed a combination of the Landauer formalism and *ab initio* simulations to calculate the Seebeck coefficient, electrical conductivity, and electronic thermal conductivity as a function of carrier concentration for both n and p-type doping. The behaviors of TE transport properties for the three MOFs can be well understood from the calculated band structures, band alignment, and partial density of states. The different electronic and thermoelectric characteristics of $X_3(HITP)_2$ 2D MOFs indicate that the intrinsic material properties strongly depend on their microscopic structure (or morphology) and chemical composition, and would largely influence the efficiency of TE devices. The calculated power factors suggest that the electronic transport properties of $X_3(HITP)_2$ could be enhanced by substituting heavy metal ions to increase the interaction between metal ion and ligands. The TE efficiency of these MOF materials (i.e. ZT) may be increased by improving the crystallinity of samples. The results of this work provide a fundamental guidance to further optimize the existing 2D MOFs, and to design and discover new families of MOF-like materials for thermoelectric applications.

METHODS

Ab initio calculation

The atomic structures of monolayer hexagonal $X_3(HITP)_2$ with X=Ni, Pd, or Pt were generated based on the experimental data for $Ni_3(HITP)_2$ [8], and then optimized using *ab initio* simulations. All electronic and structural optimization calculations were performed within the Kohn-Sham density functional theory (DFT) framework implemented in the Vienna *ab initio* simulation package (VASP)[36]. The Local Density Approximation (LDA)[37] for the exchange and correlation functional was used to describe the electrons of all atoms, except for Ni, for which the LDA+U[38] with U=6.0[39] was applied to better represent the strong correlation of the Ni *d* orbitals. Previous studies showed that the *d* orbitals of both Pd and Pt are less localized than that of Ni metal (i.e. U_{pd} =1.005 and U_{pt} =1.07)[40], hence we did not use LDA+U for Pd and Pt MOFs. We also calculated the band structures of the Pt MOF within the Generalized Gradient Approximation (GGA) using the PW91 functional including spin-orbit coupling to see the influence of relativistic effects on the band structure, and found that the calculated band structure is similar to that of LDA with a small rigid shift. The projector augmented wave (PAW) pseudo-potential[41] was chosen to describe the electron-core interactions, and a kinetic energy cutoff of 400 eV was defined for the plane-wave basis set. The Brillouin zone for all simulated systems was sampled with a Monkhorst-Pack grid[42] of 8x8x1 for both electronic structure and optimization calculations, while a grid of 16x16x1 was used for the calculations of thermal transport properties. To mimic a 2D MOF, we increased the length of the simulation cell along the Z direction up to ~8 Å to avoid image interactions. Since LDA generally underestimates the electronic band gap, HSE06[43] calculations were performed on the three 2D MOFs. All TE transport properties were calculated with the band gaps obtained using the HSE06 functional.

Thermoelectric transport model

The thermoelectric transport properties of three 2D MOFs were calculated using the Landauer formalism in the linear response regime[44]:

$$S = \left(-\frac{k_B}{e}\right)\frac{I_1}{I_0} \tag{1}$$

$$\sigma / \lambda = \frac{1}{A}\left(\frac{2e^2}{h}\right) I_0 \tag{2}$$

$$\kappa_e / \lambda = \left(\frac{1}{A}\right)\left(\frac{2k_B^2 T}{h}\right)\left(I_2 - I_1^2 / I_0\right) \tag{3}$$

$$I_j = \int \left(\frac{E-E_f}{k_B T}\right)^j \tilde{T}(E)\left(-\frac{\partial f_0}{\partial E}\right) dE \tag{4}$$

where e is the electronic charge, k_B the Boltzmann constant, h the Planck constant, T the temperature, and A the area of the simulation cell; $f_0(E) = 1/(1+e^{(E-E_f)/k_B T})$ is the Fermi-Dirac distribution function with respect to the Fermi level E_f; $\tilde{T} = T(E)M(E)$ with the transmission $T(E) = \lambda / L$, the density of tunneling modes $M(E) = (h/2L)\sum_k |v_k^\alpha| \delta(E - E_k)$ and

$\delta(E-E_k)=(1/w\sqrt{2\pi})e^{-(E-E_k)^2/2w^2}$. The ratio of the mean free path λ and the length L of the system can be used to determine the carrier transport in ballistic or diffusive regime (i.e. *T(E)* =1 for ballistic and 0<*T(E)*<1 for diffusive regime).

Using the VASP code, we calculated the group velocities of the charge carriers by using the finite difference method $v_k^y=(1/h)(\Delta E_k/\Delta k_y)$ with a small value of Δk_y along the y direction. The carrier DOS was produced by using the Gaussian smearing $\delta(E-E_k)=(1/w\sqrt{2\pi})e^{-(E-E_k)^2/2w^2}$ on a calculated full electronic band structure energy E_k with a k-point sampling of 16x16x1 over a whole Brillouin zone and a smearing width of 0.005 eV. The sum of the product of v_k^y and the DOS over all k-points yields the density of modes *M(E).*

Classical molecular dynamics calculation

Classical molecular dynamics was used to simulate the phonon modes and their interactions given an empirical interaction potential. In this context, the heat flux J is defined as

$$\boldsymbol{J}=\frac{1}{V}\sum_\alpha(\varepsilon_\alpha\boldsymbol{I}+v_\alpha^T)v_\alpha \quad (5)$$

and the thermal conductivity tensor $\boldsymbol{\kappa}$ was obtained from the Green-Kubo formula

$$\boldsymbol{\kappa}=\frac{V}{k_BT^2}\int_0^\infty\langle\boldsymbol{J}(0)\otimes\boldsymbol{J}(t)\rangle dt \quad (6)$$

where V is the system volume, ε_α is the per-atom energy, v_α^T is the per-atom virial, v_α is the velocity of atom α, T is the temperature, k_B is the Boltzmann constant, $\langle\cdot\rangle$ denotes the canonical ensemble average, and $\langle J\rangle = 0$ in equilibrium. The trajectories $\{x_\alpha(t)\}$ of the atoms were obtained by integrating Newton's equations of motion, $m_\alpha\ddot{x}_\alpha=f_\alpha$, given initial conditions, masses m_α, and forces f_α derived from an empirical potential

$$\Phi(x_\alpha,q_\alpha)=\frac{\epsilon}{2}\sum_{\alpha,\beta}\frac{q_\alpha q_\beta}{r_{\alpha\beta}^2}+\frac{1}{2}\sum_{\alpha,\beta}\varphi(r_{\alpha\beta})+\sum_\alpha \mathrm{B}_a(x_a) \quad (7)$$

where q_α is the charge on atom α, and $r_{\alpha\beta}=|\mathbf{x}_\alpha-\mathbf{x}_\beta|$ is the distance between atoms α and β. The first term is the Coulomb potential, the second is a Lennard-Jones pair potential modeled with van der Waals interactions, and the third is comprised of pair, angle, and dihedral bonds.

The partial charges q_α for the long-range Coulomb interactions were calculated with DFT/B3LYP (CRYSTAL14) via the Mulliken method on the optimized monolayer. The majority of the other parameters and functional forms of the potential were obtained from the well-known unified AMBER potential[45]. To allow for realistic anharmonic interactions and hence thermal conductivity, Morse pair bonds were used with an exponent of 2 in B_a with the equilibrium distance and stiffness matched to the harmonic bonds specified by the AMBER parameterization. The stiffness of the metal X-N pair bond and N-X-N angle bond missing from the AMBER parameterization were tuned using a frozen phonon-like method where the frequencies of a set of modes were adjusted to match those obtained from DFT/B3LYP calculations on a model system containing a single square planar metal center with diaminobenzene linkers; the system has the same N-X-N environment. The frequency of the empirical model of a given mode $\boldsymbol{m}$ was calculated via

$$\omega^2 \approx -\boldsymbol{m} \cdot \boldsymbol{M}^{-1} \frac{1}{\varepsilon} \boldsymbol{f}(\varepsilon \boldsymbol{m}) \quad (8)$$

where $\boldsymbol{M}$ is a diagonal matrix of atomic masses and $\boldsymbol{f}$ is the vector of atomic forces resulting from a displacement $\varepsilon\boldsymbol{m}$ from equilibrium with ε being a small number. The modes of the minimal substructure that have the same N-X-N coordination where used to simultaneously tune the metal X pair and angle bonds. In particular, the lowest frequency predominantly in-plane stretching and a bending modes were used since these were deemed to be the most informative of the two missing parameters.

With the interatomic potential fully specified, the Green-Kubo method was used to calculate the in-plane thermal conductivity using a rectangular unit cell. The size of the cell (2x2) was chosen based on previous results by Huang et al.[46] (and in our preliminary studies, 3x3 and 4x4 supercells gave comparable results). To obtain the ensemble average of the flux correlations given in Eq. (6), the atomic trajectories of 10 replicas, with initial velocities drawn from a Boltzmann distribution, were simulated using constant energy dynamics for 3.2 ns after equilibrating at 300 K. These simulations were done with LAMMPS. The calculated thermal conductivity for the single sheet in the armchair direction was 0.97 ± 0.03 W/mK, and 1.25 ±0.03 W/mK in the perpendicular direction, based on a sheet-to-sheet spacing of 0.3 nm.

Conflict of interest: The authors declare no competing financial interest.

ACKNOWLEDGEMENTS:

We thank Andrew Ullman and Vitalie Stavila for useful discussion. This work was supported by the Sandia Laboratory Directed Research and Development (LDRD) Program. Sandia National Laboratories is a multi-program laboratory managed and operated by Sandia Corporation, a wholly owned subsidiary of Lockheed Martin Corporation, for the U.S. Department of Energy's National Nuclear Security Administration under contract DE-AC04-94AL85000.

Table I. Optimized lattice constants and calculated band gap of $X_3(HITP)_2$ with X=Ni, Pd and Pt using DFT with both LDA and HSE06 functionals. The numbers in the parentheses are experimental values [9].

	a_x(Å)	a_y(Å)	E_g^{LDA} (eV)	E_g^{HSE06} (eV)
$Ni_3(HITP)_2$	21.32 (21.75)	21.32 (21.75)	0.07	0.25 (0.2)
$Pd_3(HITP)_2$	21.78	21.78	0.11	0.32
$Pt_3(HITP)_2$	22.06	22.06	0.27	0.42

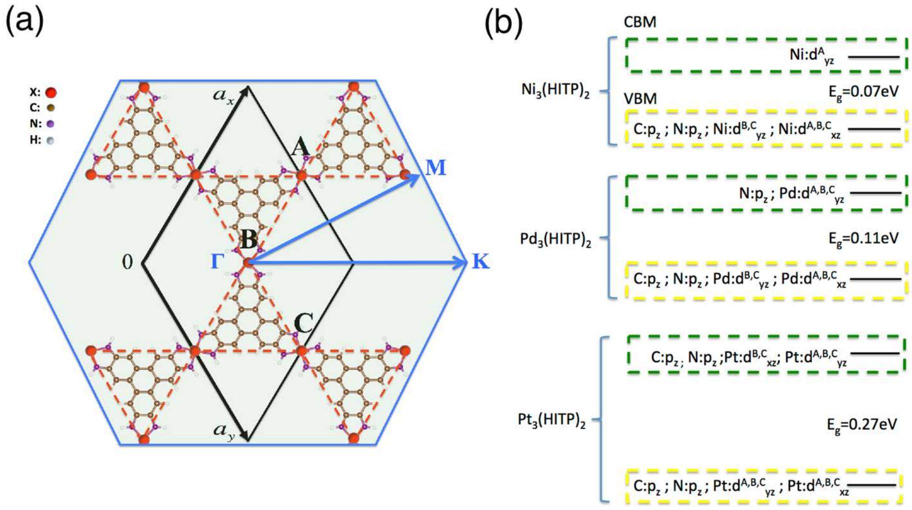

Figure 1. (a) Schematic diagram of the unit cell of $X_3\,(HITP)_2$ with lattice vectors a_x and a_y, and atomic sites A, B and C of X in the unit cell (black), and its first Brillouin zone with high symmetry points Γ, M and K (blue). (b) Schematic of the CBM (green) and VBM (yellow) for $Ni_3(HITP)_2$, $Pd_3(HITP)_2$, and $Pt_3(HITP)_2$.

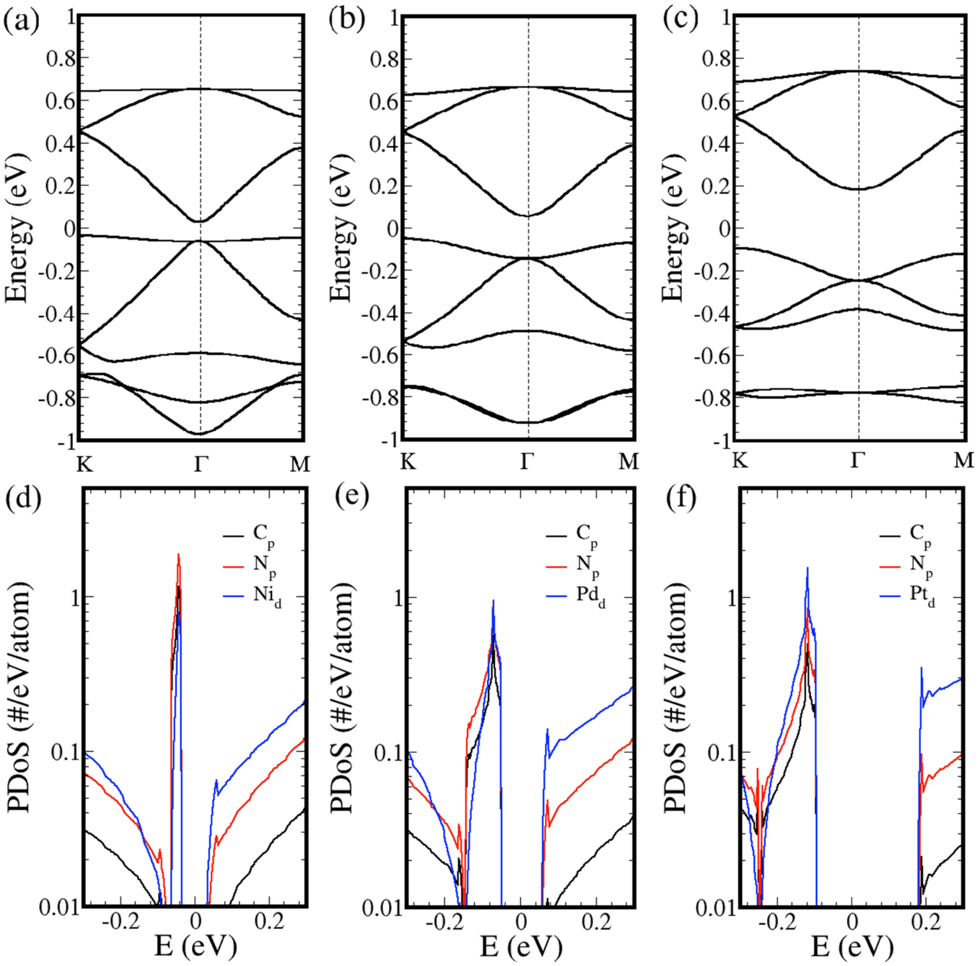

Figure 2. Calculated band structure for (a) $Ni_3(HITP)_2$, (b) $Pd_3(HITP)_2$, and (c) Pt3$(HITP)_2$. Panels (d-f) show the corresponding partial density of states contributed from the *d* orbitals of Ni (Ni_d), Pd (Pd_d) and Pt (Pt_d), and the *p* orbitals of C (C_p) and N (N_p).

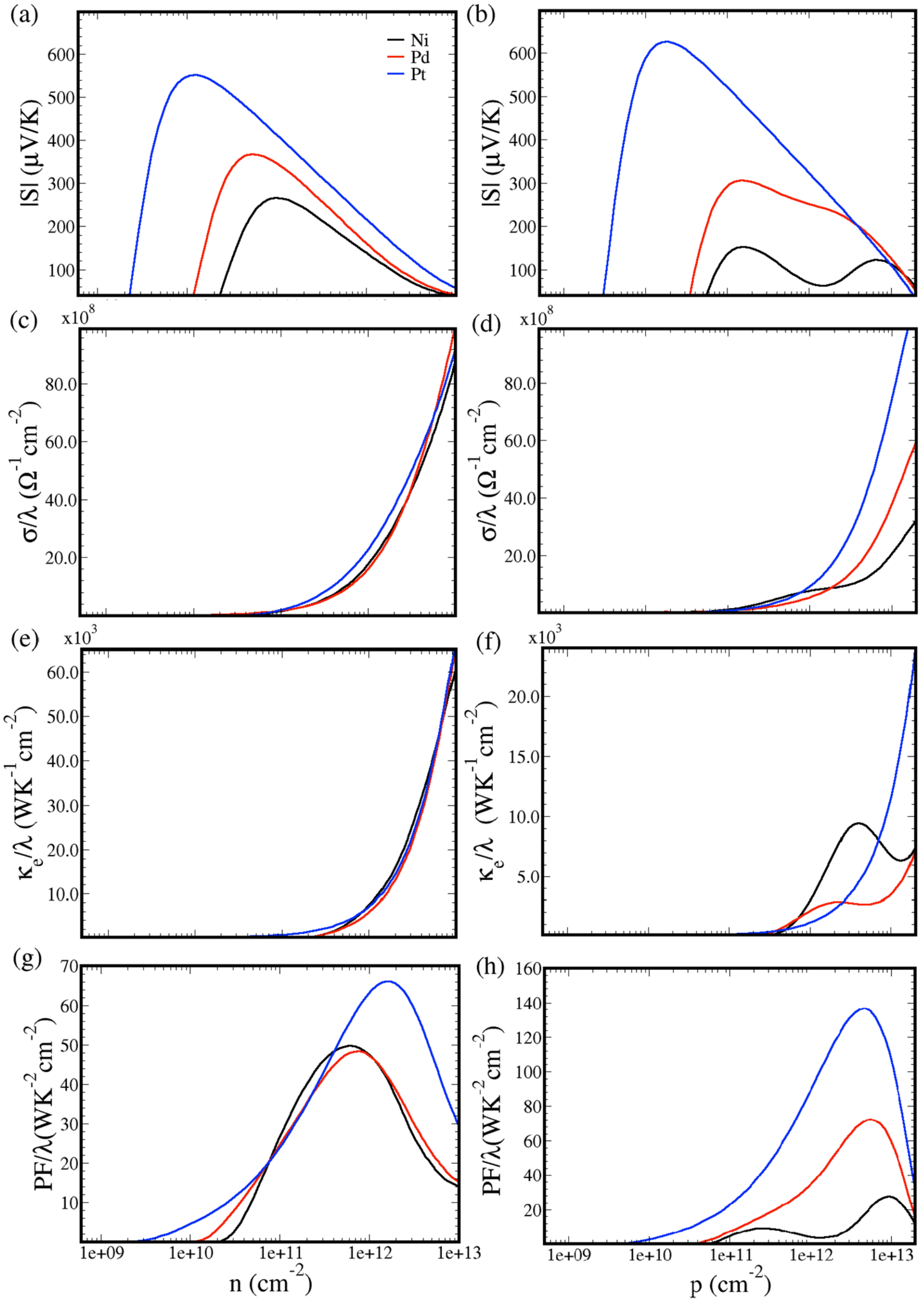

Figure 3. Calculated thermoelectric transport properties for $Ni_3(HITP)_2$ (black), $Pd_3(HITP)_2$ (red), and $Pt_3(HITP)_2$ (blue) as a function of electron (n) and hole (p) concentration. (a, b) Absolute value of Seebeck coefficient (|S|), (c, d) electrical conductivity (σ) over mean free path (λ), (e, f) electronic thermal conductivity (κ_e) over λ, and (g, h) power factor (PF) over λ at room temperature.

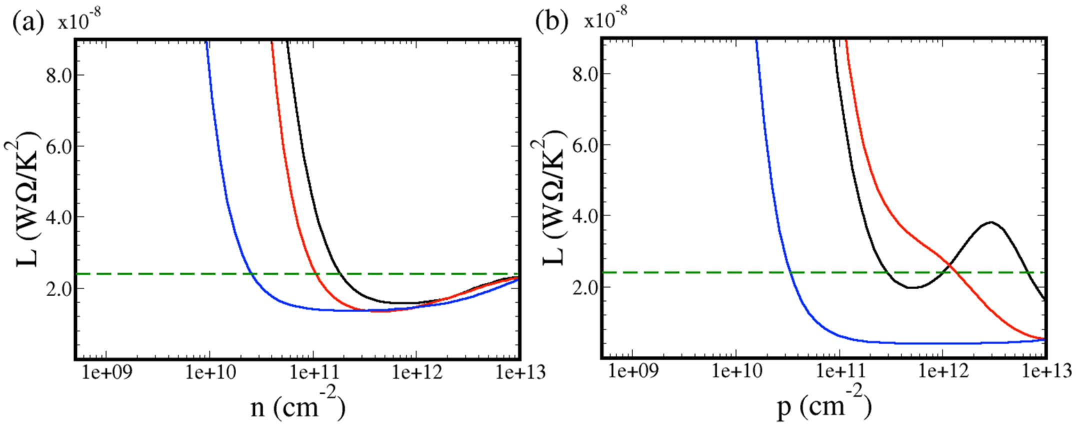

Figure 4. Calculated Lorenz number (L) as a function of electron (n) and hole (p) concentration for $Ni_3(HITP)_2$ (black), $Pd_3(HITP)_2$ (red), and $Pt_3(HITP)_2$ (blue), respectively. Green dashed line represents $L_0 = 2.4 \times 10^{-8}$ WΩ/K^2 .

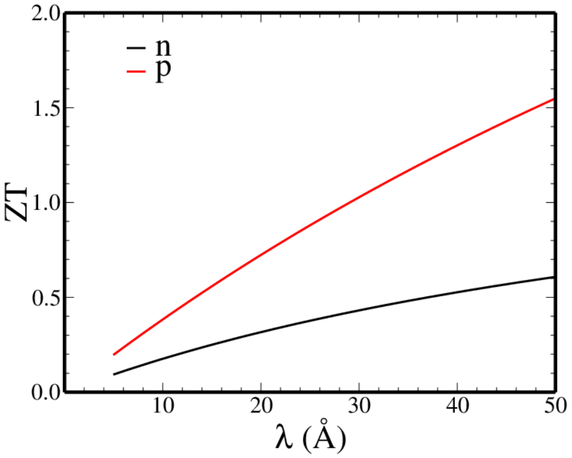

Figure 5. Calculated figure of merit ZT as a function of electronic mean free path (λ) for $Pt_3(HITP)_2$, with the carrier concentration corresponding to the peak of the power factor in Fig. 3.

REFERENCES

(1) Novoselov, K. S.; Geim, A. K.; Morozov, S. V.; Jiang, D.; Katsnelson, M. I.; Grigorieva, I. V.; Dubonos, S. V.; Firsov, A. A. Two-Dimensional Gas of Massless Dirac Fermions in Graphene. *Nature* **2005,** *438*, 197-200.

(2) Zhang, Y.; Tan, Y.-W.; Stormer, H. L.; Kim, P. Experimental Observation of the Quantum Hall Effect and Berry's Phase in Graphene. *Nature* **2005,** *438*, 201-204.

(3) Seol, J. H*., et al.* Two-Dimensional Phonon Transport in Supported Graphene. *Science* **2010,** *328*, 213-216.

(4) Wang, Q. H.; Kalantar-Zadeh, K.; Kis, A.; Coleman, J. N.; Strano, M. S. Electronics and Optoelectronics of Two-Dimensional Transition Metal Dichalcogenides. *Nat. Nanotechnol.* **2012,** *7*, 699-712.

(5) Zhu, W.; Low, T.; Lee, Y.-H.; Wang, H.; Farmer, D. B.; Kong, J.; Xia, F.; Avouris, P. Electronic Transport and Device Prospects of Monolayer Molybdenum Disulphide Grown by Chemical Vapour Deposition. *Nat Commun* **2014,** *5*, 3087.

(6) Wang, G*., et al.* Spin-Orbit Engineering in Transition Metal Dichalcogenide Alloy Monolayers. *Nat. Commun.* **2015,** *6*, 10110.

(7) Klee, V*., et al.* Superlinear Composition-Dependent Photocurrent in CVD-Grown Monolayer $MoS_{2(1-x)}Se_{2x}$ Alloy Devices. *Nano Lett.* **2015,** *15*, 2612-2619.

(8) Sheberla, D.; Sun, L.; Blood-Forsythe, M. A.; Er, S.; Wade, C. R.; Brozek, C. K.; Aspuru-Guzik, A.; Dincă, M. High Electrical Conductivity in Ni_3(2,3,6,7,10,11-Hexaiminotriphenylene)$_2$, a Semiconducting Metal–Organic Graphene Analogue. *J. Am. Chem. Soc.* **2014,** *136*, 8859-8862.

(9) Dong, L.; Kim, Y.; Er, D.; Rappe, A. M.; Shenoy, V. B. Two-Dimensional Pi-Conjugated Covalent-Organic Frameworks as Quantum Anomalous Hall Topological Insulators. *Phys. Rev. Lett.* **2016,** *116*, 096601.

(10) Foster, M. E.; Sohlberg, K.; Spataru, C. D.; Allendorf, M. D. Proposed Modification of the Graphene Analogue $Ni_3(Hitp)_2$ to Yield a Semiconducting Material. *J. Phys. Chem. C* **2016,** *120*, 15001-15008.

(11) Chen, S.; Dai, J.; Zeng, X. C. Metal-Organic Kagome Lattices M_3(2,3,6,7,10,11-Hexaiminotriphenylene)$_2$ (M = Ni and Cu): From Semiconducting to Metallic by Metal Substitution. *Phys. Chem. Chem. Phys.* **2015,** *17*, 5954-5958.

(12) Tritt, T. M. Thermoelectric Phenomena, Materials, and Applications. *Annu. Rev. Mater. Res.* **2011,** *41*, 433-448.

(13) Snyder, G. J.; Toberer, E. S. Complex Thermoelectric Materials. *Nat. Mater.* **2008,** *7*, 105-114.

(14) Zhang, X.; Zhao, L.-D. Thermoelectric Materials: Energy Conversion between Heat and Electricity. *J. Materiomics* **2015,** *1*, 92-105.

(15) Slack, G. A., New Materials and Performance Limits for Thermoelectric Cooling. In *Crc Handbook of Thermoelectrics*, CRC Press: 1995.

(16) Tsai, T.-C.; Chang, H.-C.; Chen, C.-H.; Huang, Y.-C.; Whang, W.-T. A Facile Dedoping Approach for Effectively Tuning Thermoelectricity and Acidity of Pedot:Pss Films. *Org. Electron.* **2014,** *15*, 641-645.

(17) Park, T.; Park, C.; Kim, B.; Shin, H.; Kim, E. Flexible Pedot Electrodes with Large Thermoelectric Power Factors to Generate Electricity by the Touch of Fingertips. *Energy Environ. Sci.* **2013,** *6*, 788-792.

(18) Bubnova, O.; Khan, Z. U.; Malti, A.; Braun, S.; Fahlman, M.; Berggren, M.; Crispin, X. Optimization of the Thermoelectric Figure Of merit in the Conducting Polymer Poly(3,4-Ethylenedioxythiophene). *Nat. Mater.* **2011,** *10*, 429-433.

(19) Bubnova, O.; Crispin, X. Towards Polymer-Based Organic Thermoelectric Generators. *Energy Environ. Sci.* **2012,** *5*, 9345-9362.

(20) Kim, G. H.; Shao, L.; Zhang, K.; Pipe, K. P. Engineered Doping of Organic Semiconductors for Enhanced Thermoelectric Efficiency. *Nat. Mater.* **2013,** *12*, 719-723.

(21) Cahill, D. G.; Pohl, R. O. Thermal Conductivity of Amorphous Solids above the Plateau. *Phys. Rev. B* **1987,** *35*, 4067-4073.

(22) Jiang, F.-X.; Xu, J.-K.; Lu, B.-Y.; Xie, Y.; Huang, R.-J.; Li, L.-F. Thermoelectric Performance of Poly(3,4-Ethylenedioxythiophene): Poly(Styrenesulfonate). *Chin. Phys. Lett.* **2008,** *25*, 2202.

(23) Yan, H.; Sada, N.; Toshima, N. Thermal Transporting Properties of Electrically Conductive Polyaniline Films as Organic Thermoelectric Materials. *J. Therm. Phys. Calorim.* **2002,** *69*, 881-887.

(24) D'Alessandro, D. M.; Kanga, J. R. R.; Caddy, J. S. Towards Conducting Metal-Organic Frameworks. *Aust. J. Chem.* **2011,** *64*, 718-722.

(25) Sun, L.; Miyakai, T.; Seki, S.; Dincă, M. Mn_2(2,5-Disulfhydrylbenzene-1,4-Dicarboxylate): A Microporous Metal–Organic Framework with Infinite (−Mn–S−)∞ Chains and High Intrinsic Charge Mobility. *J. Am. Chem. Soc.* **2013,** *135*, 8185-8188.

(26) Talin, A. A., *et al.* Tunable Electrical Conductivity in Metal-Organic Framework Thin-Film Devices. *Science* **2014,** *343*, 66-69.

(27) Sun, L.; Campbell, M. G.; Dincă, M. Electrically Conductive Porous Metal–Organic Frameworks. *Angew. Chem. Int. Edit.* **2016,** *55*, 3566-3579.

(28) Butler, K. T.; Hendon, C. H.; Walsh, A. Electronic Chemical Potentials of Porous Metal–Organic Frameworks. *J. Am. Chem. Soc.* **2014,** *136*, 2703-2706.

(29) Cox, P. A., *The Electronic Structure and Chemistry of Solids*. Oxford University Press: New York, 1987.

(30) Landauer, R. Electrical Resistance of Disordered One-Dimensional Lattices. *Philos. Mag.* **1970,** *21*, 863-867.

(31) Landauer, R. Spatial Variation of Currents and Fields Due to Localized Scatterers in Metallic Conduction. *IBM J. Res. Dev.* **1957,** *1*.

(32) Jeong, C.; Kim, R.; Luisier, M.; Datta, S.; Lundstrom, M. On Landauer Versus Boltzmann and Full Band Versus Effective Mass Evaluation of Thermoelectric Transport Coefficients. *J. Appl. Phys.* **2010,** *107*, 023707.

(33) Goldsmid, H. J.; Sharp, J. W. Estimation of the Thermal Band Gap of a Semiconductor from Seebeck Measurements. *J. Electron. Mater.* **1999,** *28*, 869-872.

(34) Wei, P.; Bao, W.; Pu, Y.; Lau, C. N.; Shi, J. Anomalous Thermoelectric Transport of Dirac Particles in Graphene. *Phys. Rev. Lett.* **2009,** *102*, 166808.

(35) Wu, J.; Schmidt, H.; Amara, K. K.; Xu, X.; Eda, G.; Özyilmaz, B. Large Thermoelectricity Via Variable Range Hopping in Chemical Vapor Deposition Grown Single-Layer MoS_2. *Nano Lett.* **2014,** *14*, 2730-2734.

(36) Kresse, G.; Furthmuller, J. Efficient Iterative Schemes for Ab Initio Total-Energy Calculations Using a Plane-Wave Basis Set. *Phys. Rev. B* **1996,** *54*, 11169-11186.

(37) Perdew, J. P.; Zunger, A. Self-Interaction Correction to Density-Functional Approximations for Many-Electron Systems. *Phys. Rev. B* **1981,** *23*, 5048-5079.

(38) Dudarev, S. L.; Botton, G. A.; Savrasov, S. Y.; Humphreys, C. J.; Sutton, A. P. Electron-Energy-Loss Spectra and the Structural Stability of Nickel Oxide: An Lsda+U Study. *Phys. Rev. B* **1998,** *57*, 1505-1509.

(39) Jain, A.; Hautier, G.; Moore, C. J.; Ping Ong, S.; Fischer, C. C.; Mueller, T.; Persson, K. A.; Ceder, G. A High-Throughput Infrastructure for Density Functional Theory Calculations. *Comput. Mater. Sci.* **2011,** *50*, 2295-2310.

(40) Povzner, A. A.; Volkov, A. G.; Filanovich, A. N. Electronic Structure and Magnetic Susceptibility of Nearly Magnetic Metals (Palladium and Platinum). *Phys. Solid State* **2010,** *52*, 2012-2018.

(41) Blochl, P. E. Projector Augmented-Wave Method. *Phys. Rev. B* **1994,** *50*, 17953-17979.

(42) Monkhorst, H. J.; Pack, J. D. Special Points for Brillouin-Zone Integrations. *Phys. Rev. B* **1976,** *13*, 5188-5192.

(43) Heyd, J.; Scuseria, G. E.; Ernzerhof, M. Hybrid Functionals Based on a Screened Coulomb Potential. *J. Chem. Phys.* **2003,** *118*, 8207-8215.

(44) Kim, R.; Datta, S.; Lundstrom, M. S. Influence of Dimensionality on Thermoelectric Device Performance. *J. Appl. Phys.* **2009,** *105*, 034506.

(45) Cornell, W. D.; Cieplak, P.; Bayly, C. I.; Gould, I. R.; Merz, K. M.; Ferguson, D. M.; Spellmeyer, D. C.; Fox, T.; Caldwell, J. W.; Kollman, P. A. A Second Generation Force Field for the Simulation of Proteins, Nucleic Acids, and Organic Molecules. *J. Am. Chem. Soc.* **1995,** *117*, 5179-5197.

(46) Huang, B. L.; McGaughey, A. J. H.; Kaviany, M. Thermal Conductivity of Metal-Organic Framework 5 (Mof-5): Part I. Molecular Dynamics Simulations. *Int. J. Heat Mass Transfer* **2007,** *50*, 393-404.